# Structure and variances of equatorial zonal circulation in a multimodel ensemble

**B. Yu · F. W. Zwiers · G. J. Boer · M. F. Ting**

**Abstract** The structure and variance of the equatorial zonal circulation, as characterized by the atmospheric mass flux in the equatorial zonal plane, is examined and inter-compared in simulations from 9 CMIP3 coupled climate models with multiple ensemble members and the NCEP-NCAR and ERA-40 reanalyses. The climate model simulations analyzed here include twentieth century (20C3M) and twenty-first century (SRES A1B) simulations. We evaluate the 20C3M modeled zonal circulations by comparing them with those in the reanalyses. We then examine the variability of the circulation, its changes with global warming, and the associated thermodynamic maintenance. The tropical zonal circulation involves three major components situated over the Pacific, Indian, and Atlantic oceans. The three cells are supported by the corresponding diabatic heating extending deeply throughout the troposphere, with heating centers apparent in the mid-troposphere. Seasonal features appear in the zonal circulation, including variations in its intensity and longitudinal migration. Most models, and hence the multi-model mean, represent the annual and seasonal features of the circulation and the associated heating reasonably well. The multi-model mean reproduces the observed climatology better than any individual model, as indicated by the spatial pattern correlation and mean square difference of the mass flux and the diabatic heating compared to the reanalysis based values. Projected changes in the zonal circulation under A1B forcing are dominated by mass flux changes over the Pacific and Indian oceans. An eastward shift of the Pacific Walker circulation is clearly evident with global warming, with anomalous rising motion apparent over the equatorial central Pacific and anomalous sinking motions in the west and east, which favors an overall strengthening of the Walker circulation. The zonal circulation weakens and shifts westwards over the Indian Ocean under external forcing, whereas it strengthens and shifts slightly westwards over the Atlantic Ocean. The forced circulation changes are associated with broad SST and atmospheric diabatic heating changes in the tropics. Linear trends of these forced circulation changes, as characterized by regional spatial maximum amplitudes of mass fluxes and their longitudes over the three oceans, are statistically significant at the 5 % level for 2000–2099 for the multi-model mean. However, wide differences of the trends are apparent across the models, because of both deficiencies in the simulation of the circulations in different models and the high internal variability of the circulations.

**Keywords** Tropical zonal circulation · Variability · Climate change · Thermodynamic maintenance

B. Yu (✉)
Climate Data and Analysis Section,
Climate Research Division, Environment Canada,
4905 Dufferin Street, Toronto, ON M3H 5T4, Canada
e-mail: bin.yu@ec.gc.ca

F. W. Zwiers
Pacific Climate Impacts Consortium,
University of Victoria, Victoria, BC, Canada

G. J. Boer
Canadian Centre for Climate Modeling and Analysis,
Climate Research Division, Environment Canada,
Victoria, BC, Canada

M. F. Ting
Lamont-Doherty Earth Observatory,
Columbia University, Palisades, NY, USA

## 1 Introduction

The observed variability and change in tropical atmospheric meridional circulations, and its representation in climate simulations used in IPCC (intergovernmental panel on climate change) reports, have been investigated extensively (e.g., Knutson and Manabe 1995; Quan et al. 2004; Mitas and Clement 2005, 2006; Walker and Schneider 2006; Lu et al. 2007; Ma and Li 2008; Gastineau et al. 2009). However, relatively few studies have focused on changes in the tropical zonal circulations.

Betts and Ridgway (1989) and Betts (1998) demonstrate that the weakening of the tropical large-scale circulation has important consequences for the hydrologic cycle. Held and Soden (2006) further demonstrate that greenhouse gas increases should weaken large scale atmospheric circulations due to the different responses of global mean precipitation and water vapor in the lower troposphere under global warming. Observational evidence consistent with a weakened Walker circulation over the twentieth century has been provided in previous studies (e.g., Vecchi and Soden 2007, and references therein), including an overall tendency to "El Niño-like" conditions (e.g., Trenberth and Hurrell 1994; Graham 1994; Zhang et al. 1997; Deser et al. 2004), changes in observed sea level pressure and windstress (e.g., Zhang and Song 2006; Vecchi et al. 2006), changes in different kinds of proxy data (e.g., Urban et al. 2000; Cobb et al. 2001; Clarke and Lebedev 1997; Vecchi et al. 2006), and changes in the atmospheric mass flux (e.g., Yu and Zwiers 2010).

A slow-down of the Walker circulation is also seen in climate change simulations generated for the IPCC assessment reports, including changes in dry static stability and radiative cooling of the troposphere (e.g., Knutson and Manabe 1995; Sugi et al. 2002), and changes in the divergent circulation (e.g., Yu and Boer 2002; Tanaka et al. 2004; Gastineau et al. 2009) and stationary eddies of the vertical velocity at 500 hPa (Vecchi and Soden 2007). Over the tropical region, the atmospheric circulation changes with global warming act to weaken the background vertical motion, except over the central equatorial Pacific, where an eastward shift in convection acts to reinforce the background ascending motion (Vecchi and Soden 2007).

Relevant changes have also been reported in the circulation anomalies associated with El Niño in changing climates. Several recent studies demonstrate that the canonical eastern Pacific El Niño (EP-El Niño) has become less frequent and a different kind of El Niño (termed the central Pacific El Niño, CP-El Niño) has become more common during the late twentieth century and in several global warming simulations (e.g., Trenberth and Stepaniak 2001; and Yeh et al. 2009). The CP-El Niño has increased

sea surface temperature (SST) anomalies in the central Pacific, sandwiched by anomalous cooling in the east and west (Ashok and Yamagata 2009), leading to two opposing circulation anomalies over the equatorial Pacific.

The purpose of this study is to analyze the structure and variance of atmospheric mass fluxes along the equator, which is directly related to the tropical thermally driven zonal circulation, in the CMIP3 (Phase 3 of the Coupled Model Intercomparison Project) multi-model collection of climate simulations. In particular, we examine the vertical structure and evolution of the simulated zonal circulation, the variance of the circulation, the change of the circulation with global warming, and the associated thermodynamic maintenance. We evaluate the modeled three-dimensional circulations by comparing them with corresponding results calculated from two reanalyses. We compare the internal variability and forced responses of the modeled circulations as well as the inter-model variability related to model structure, and focus on the spatial change and temporal evolution of the circulations under external forcing. We evaluate the relative agreement between the climate model and reanalysis results and the agreement between individual models. The influence of ENSO (El Niño-Southern Oscillation) variability on the zonal circulations is also briefly discussed.

## 2 Data and analysis methods

### 2.1 Climate model simulations and reanalysis data

Our diagnoses are based on the CMIP3 multi-model dataset (available at http://www-pcmdi.llnl.gov/ipcc/about_ipcc.php), the NCEP-NCAR (National Centers for Environmental Prediction–National Center for Atmospheric Research) reanalysis (referred to as NCEP, Kistler et al. 2001) and the ECMWF (European Centre for Medium-Range Weather Forecasts) ERA-40 reanalysis (Uppala et al. 2005). We consider 9 climate models for which at least three realizations are available for both the twentieth century (20C3M) and the twenty-first century using the SRES A1B emissions scenario; the models are CCCma/C3T47, GISS/AOM, GISS/ER, IAP/FGOALS-g1.0, NIES/MIROC3.2-medres, MPI/ECHAM5, MRI/C2.3.2, NCAR/CCSM3.0, and NCAR/PCM1. Descriptions of the model configurations, including atmosphere and ocean resolutions and coupling strategies, can be found on the above website and are summarized in Meehl et al. (2007a). For each model, we use the first three 20C3M simulations and the three corresponding A1B simulations. We examine the climate simulations for the 200-year period from September 1900 to August 2100 (1900–2099). We consider September to the following August as 1 year in this analysis, and label

years according to the September dates. The variables used are monthly mean fields including three dimensional (3D) velocities and temperature in the troposphere and SST. All variables are interpolated to a standard $5° \times 5°$ grid.

Atmospheric mass fluxes calculated from the reanalyses and model outputs are used to evaluate the climate model simulated tropical zonal circulation climatology. The period of the reanalyses used for comparison is September 1957 to August 2002 (1957–2001), which is the period that is common to both reanalyses. There are known inhomogeneities in the NCEP reanalysis that are related to improvements in the measurement technique and in the reanalysis model (Kistler et al. 2001; see also the NCEP problems listed at http://www.cdc.noaa.gov/data/reanalysis/problems.shtml). Nevertheless, results of the large scale circulation and the associated diabatic heating as shown below are generally consistent in the two reanalyses (also see Yu and Zwiers 2010).

## 2.2 Diagnostic methods

The tropical circulation is primarily thermally driven. The equatorial zonal circulation can therefore be well approximated by the thermally driven divergent component of the atmospheric flow in the equatorial zonal plane (e.g., Yu and Boer 2002). The structure of the tropical diabatic heating is examined to help understand the maintenance of the zonal circulation. The 3D diabatic heating is diagnosed as a residual from the time-averaged thermodynamic equation (e.g., Hoskins et al. 1989; Nigam 1994).

To estimate the relative importance of the internal and externally forced variances of the model circulations, we decompose the total variance of mass fluxes into three components, the internal variance, the externally forced variance and the model structure related variance (e.g., Zwiers 1996; von Storch and Zwiers 1999; Ting et al. 2009). The ENSO variability is represented by the first EOF (Empirical orthogonal function) of the tropical Pacific SST anomalies.

The linear and cubic trend components for time series of interest are calculated using normalized orthogonal polynomial approximations (e.g., Hildebrand 1956, Chap. 7). The $t$ test is used to assess whether differences between time series or linear trends are statistically significant, and the $F$ test is used to assess whether differences in variances between time series are statistically significant (e.g., von Storch and Zwiers 1999). The relative agreement between climate models and reanalyses, and between individual models, is evaluated using second-order space–time climate difference statistics (Boer and Lambert 2001).

# 3 Annual mean of the zonal circulation

## 3.1 Structure of zonal circulations and diabatic heating

The equatorial planetary scale circulation is approximated by the thermally driven divergent component of atmospheric flow in terms of the streamfunction $\psi = a\Delta\phi \int_0^p u_D dp/g$, where $u_D$ denotes the divergent component of the zonal wind, $p$ is the pressure, $g$ is the acceleration due to gravity, $a$ is the radius of the Earth, and $\Delta\varphi$ is the width of the band 5°S–5°N along the equator in radians (e.g., Yu and Boer 2002). The divergent component of the zonal wind is obtained by solving the Poisson equation globally for the potential function with divergence as the forcing term, and then calculating the divergent wind. The mass flux $\psi$ is computed subsequently by vertically integrating the divergent wind from 10 to 1,000 hPa.

The 3D diabatic heating $Q$ is diagnosed as a residual from the time-averaged thermodynamic equation. In the tropics, the thermodynamic equation may be simplified to a balance between diabatic heating and adiabatic cooling (e.g., Mitas and Clement 2006). Thus $Q \approx (p/p_0)^\kappa \omega(\frac{\partial\theta}{\partial p})$, where $p_o = 1,000$ hPa, $\kappa = 0.286$, $\omega$ is the vertical velocity, and $\theta$ is the potential temperature. The robustness of the diagnosed values of $Q$ was assessed by comparing with results reported in previous studies (e.g., Yu and Zwiers 2010).

The climatological annual means (September–August) of atmospheric mass flux $\psi$ along the equator are displayed in the upper and lower panels of Fig. 1 for the mean of the NCEP and ERA-40 reanalyses and for the 20C3M multi-model mean, respectively. Figure 2 shows the corresponding diabatic heating $Q$. Results above 100 hPa are not shown because $\psi$ is small there. The results are based on the 45-year averages of $\psi$ and $Q$ spanning from 1957 to 2001 for the reanalysis, and the 50-year averages from 1950 to 1999 for the climate models.

As described in previous studies (e.g., Peixoto and Oort 1992), the tropical zonal circulation involves three major components (Fig. 1); the Pacific Walker cell (POC) with a broad region of intense rising motion over the western-central Pacific and strong sinking motion in the eastern equatorial Pacific, a cell rising over the Indian Archipelago and sinking over the western Indian Ocean (IOC), and a cell rising over the Amazon region and sinking over the eastern equatorial Atlantic (AOC). These three circulations are directly supported by the corresponding diabatic heating extending deeply throughout the troposphere, with heating centers apparent in the mid-troposphere (Fig. 2). The diabatic heating from the simplified estimation (Fig. 2, upper panel) bears close resemblance to the result calculated from a residual of the time-averaged thermodynamic

**Fig. 1** Longitude-height planes of climatological annual means of atmospheric mass fluxes along the equator (averaged from 5°S–5°N) for the mean of NCEP and ERA-40 reanalyses from 1957 to 2001 (*upper panel*) and the multi-model mean from 1950 to 1999 (*lower panel*). Contour interval is $3.0 \times 10^9$ kgs$^{-1}$. *Block lines* indicate land areas
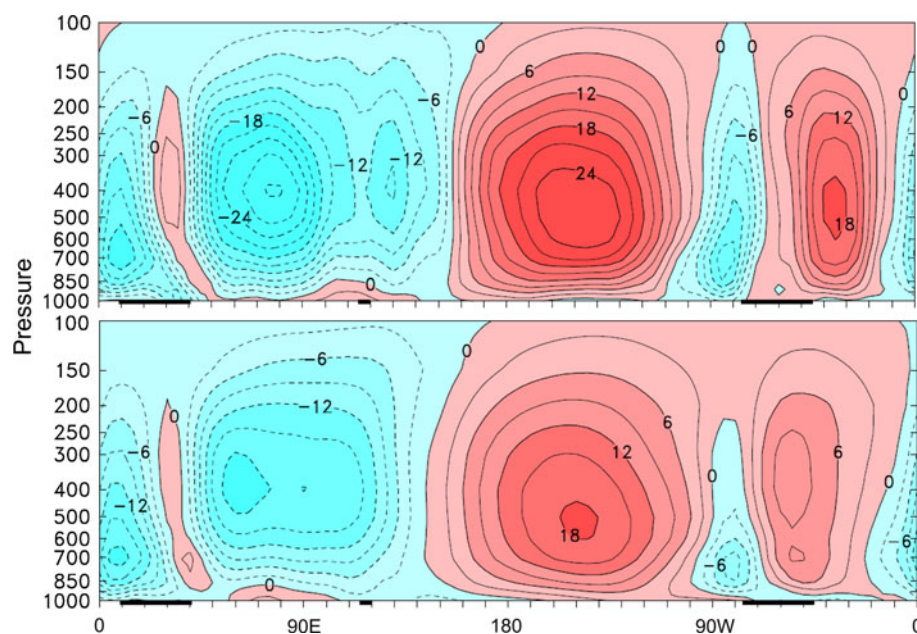


**Fig. 2** As in Fig. 1, but for the diabatic heating. Contour interval is $0.5 \times 10^{-1}$K/day
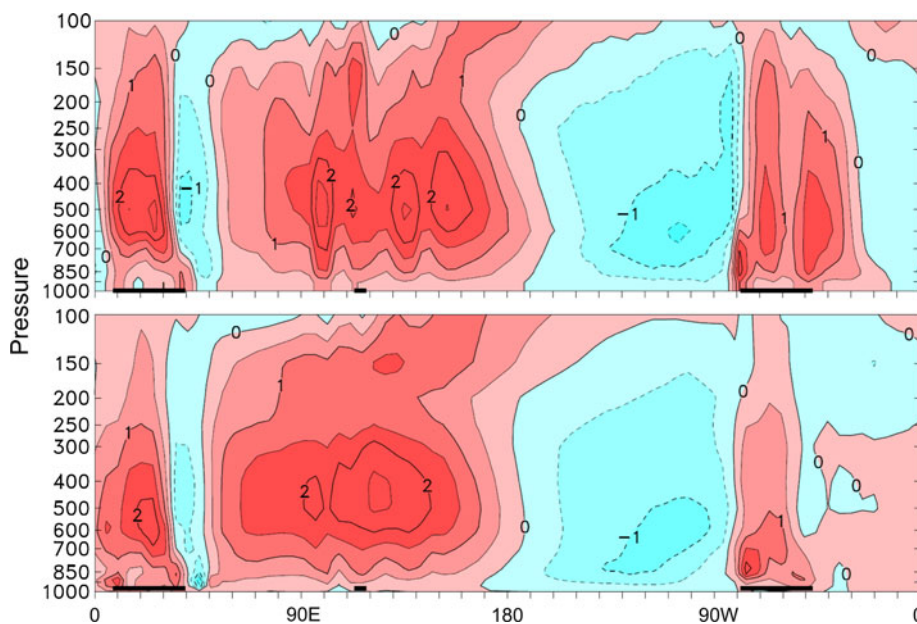


equation (Fig. 3 in Yu and Zwiers 2010), indicating a good balance between diabatic heating and adiabatic cooling in the tropics.

The multi-model result is generally smoother than that from the reanalysis, as expected due to the large number (27) of model simulations used. Nevertheless, the correspondence between the two products is rather good. The spatial pattern correlation coefficient between the two products for $\psi$ is high (up to 0.93) within the domain of interest shown in Fig. 1, although there are discrepancies in the detailed placement of the mass flux centers over the equatorial Indian and Atlantic Oceans. The spatial pattern correlation is 0.83 for the diabatic heating, lower than that for the mass flux. However, the magnitude of tropical heating is comparable in the multi-model mean and the mean of the two reanalyses, except for the heating over the Amazon region. This suggests that the tropical large-scale heating maintenance of the circulations is well reproduced overall by the mean model. Nevertheless, discrepancies in the heating structure are apparent among the models, as is discussed below.

The representation of the climatological circulation pattern is generally consistent across the models. The primary differences in the spatial distribution of $\psi$ for the

**Fig. 3** BLT diagrams illustrating the relative mean square difference (*blue scale*), the ratio of the modeled to reanalyzed variance (*green scale*), and the spatial pattern correlation between model and reanalysis components (*magenta scale*) of mass fluxes (*left panel*) and diabatic heating (*right panel*) along the equator. The reanalyzed components are the means of NCEP and ERA-40. The mean model result is also shown
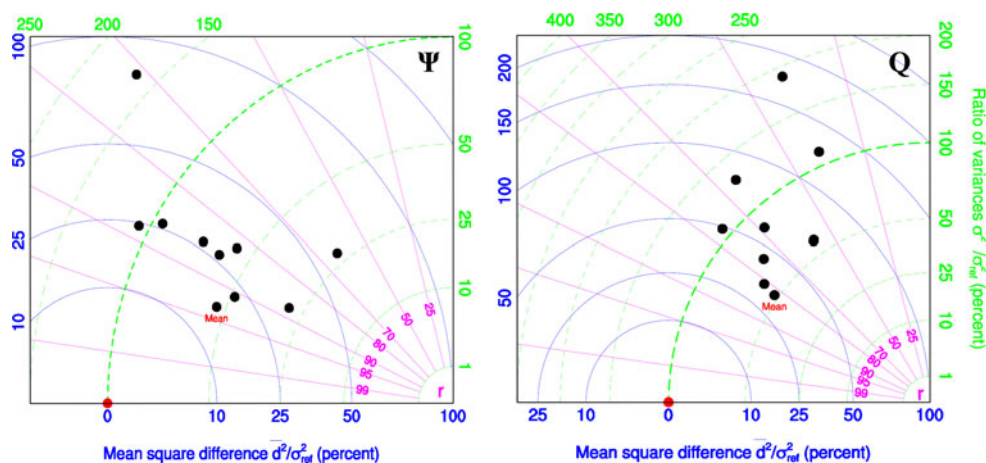
individual models are in intensity rather than the spatial distribution (not shown). The standard deviations of the climatological mass flux maxima across models are $4.1 \times 10^9$ kgs$^{-1}$ for the POC, $3.9 \times 10^9$ kgs$^{-1}$ for the IOC, and $3.2 \times 10^9$ kgs$^{-1}$ for the AOC. These values compare to multi-model mean mass flux maxima of $18.8 \times 10^9$ kgs$^{-1}$, $-19.6 \times 10^9$ kgs$^{-1}$, and $10.7 \times 10^9$ kgs$^{-1}$, respectively. The relative agreement of individual model-based $\psi$ and $Q$ patterns with the average of the reanalyses is further evaluated in Fig. 3 using the BLT diagram (Boer and Lambert 2001; a modified Taylor diagram). The diagram displays the second-order space–time climate difference statistics. Quantities in the figure are scaled by the average of NCEP and ERA-40 variances to give relative values. The relative mean-squared differences between observed and simulated climatologies are plotted on the horizontal scale. The origin, which is plotted as the red dot, indicates the observed climatology (i.e., the mean of the two reanalyses). In addition, the variance ratio and the effective correlation are indicated on the two radial scales (see Boer and Lambert 2001, for details). Individual black dots show statistics for individual models, while the black dot labelled "mean" shows the corresponding spatial statistics for the multi-model mean.

Pattern correlations for the pressure-weighted mass flux (Fig. 3, left panel) range from 0.61 to 0.91 with a value of 0.93 for the multi-model mean. However, most models have considerably lower spatial variance than either reanalysis as is seen from the ratio of variances for simulated and reanalyzed $\psi$ (the green numbers and dashed green circles in Fig. 3), although two models have values near one (i.e., 100 %) and one model has a value above one. Thus the models' spatial mass flux patterns are generally flatter than reanalysis based values as reflected in the mean. The correlation between the multi-model mean $\psi$ and the reanalysis mean is slightly higher than correlations between the individual model $\psi$'s and the reanalysis mean. Correspondingly, the mean square difference between the

multi-model mean $\psi$ and the reanalysis mean is slightly lower than those between the individual models and the reanalysis mean. These results suggest that the mean model is generally the best 'model' measured in these senses, although this is not the case when considering the ratio of spatial variances for model and reanalysis circulations.

Pattern correlations for the diabatic heating $Q$ (Fig. 3, right panel), which are generally lower than those for mass flux, range from 0.40 to 0.82 with a value of 0.83 for the multi-model mean. The spatial distribution of the diabatic heating varies considerably from model to model, in both intensity and vertical structure. Some models show strong convective heating extending high up to the upper troposphere (not shown). Consequently, the models exhibit both more or less simulated spatial variability of $Q$ than diagnosed from the reanalysis. As with $\psi$, the mean model is the best 'model' as measured by the spatial pattern correlation and the mean square difference from reanalysis, although the mean model has weak spatial variance as would be expected from ensemble averaging.

Overall, most models capture the equatorial zonal circulations and the associated heating structures seen in the reanalyses reasonably well. The mean model has the best spatial pattern correlation and the smallest mean square difference compared to the reanalysis based values.

### 3.2 Internal and forced variances

The total variance of the annual mean mass flux ($\sigma^2$) that is presented in the ensemble of climate simulations may be decomposed into three components: a component $\sigma_I^2$ that reflects internal variability, a component $\sigma_F^2$ that contains the effects of external forcing; hereafter, "forced" variance, and the model structure related variance ($\sigma_M^2$), denoting as $\sigma^2 = \sigma_I^2 + \sigma_F^2 + \sigma_M^2$ (e.g., Zwiers 1996; von Storch and

Zwiers 1999; Ting et al. 2009). The three variance components are calculated respectively as $\sigma_I^2 = \frac{1}{TM(N-1)} \sum_t \sum_m \sum_n (\psi_{tmn} - \bar{\psi}_{tm})^2$, $\sigma_F^2 = \frac{1}{(T-1)M} \sum_t \sum_m (\bar{\psi}_{tm} - \bar{\bar{\psi}}_m)^2$ and $\sigma_M^2 = \frac{1}{M-1} \sum_m (\bar{\bar{\psi}}_m - \tilde{\psi})^2$, where $\psi_{tmn}$ is the atmospheric mass flux for year $t$ ($t = 1, \ldots, T$), model $m$ ($m = 1, \ldots, M$), and ensemble member $n$ ($n = 1, \ldots, N$); $\bar{\psi}_{tm} = \frac{1}{N} \sum_n \psi_{tmn}$ is the averaged mass flux across ensemble members for year $t$ and model $m$; $\bar{\bar{\psi}}_m = \frac{1}{TN} \sum_t \sum_n \psi_{tmn}$ is the time and ensemble member averaged mass flux for each model; and $\tilde{\psi} = \frac{1}{TMN} \sum_t \sum_m \sum_n \psi_{tmn}$ is the mean mass flux with the average of all the modeled mass fluxes considered. $T = 50$ is the total number of years considered; $M = 9$ is the total number of models; and $N = 3$ is the number of ensemble members for each model. It is noted that $\sigma_M^2$, which quantifies differences between model means, is not particularly physically meaningful, in contrast with $\sigma_I^2$ and $\sigma_F^2$. It should also be noted that the forced component, $\sigma_F^2$, contains contributions from both the response to external forcing and internal variability. The latter diminishes as a function of $N^{-1}$, and thus remains substantial for the small ensembles considered in this study. The primary reason for separating $\sigma_F^2$ from the total variability is to ensure that the internal variability term $\sigma_I^2$ is not contaminated by the secular variability that results from external forcing.

Figure 4 displays the internal and forced variances, and the ratios of forced variance and internal variance calculated for two 50-year periods, 1950–1999 based on the 20C3M simulations and 2050–2099 based on the A1B simulations. The internal variance $\sigma_I^2$, which is similar in both periods, features high values over the Indian Ocean and the western-central Pacific, suggesting that the temporal circulation variance is dominated by variation in the intensity of the IOC and zonal migration of the POC along the equator. The forced variance $\sigma_F^2$ resembles the internal variance, but is weaker in magnitude. The $\sigma_F^2$ to $\sigma_I^2$ ratio is used to test whether there is a statistically significant forced signal (and where) in either of the periods. The test statistic we use is $F = N(\sigma_F^2/\sigma_I^2)$, which would nominally have an F-distribution with $(T-1)M$ and $TM(N-1)$ degrees of freedom (DF) under the null hypothesis that there is no response to external forcing. If we discount for serial correlation by dividing the number of time-related DF by 5 (a conservative assumption), then we would compare F against critical values for the F-distribution with $(T/5-1)M$ and $TM(N-1)/5$ DF, or 81 and 180 DF. The upper 5 % critical point for such an F-ratio is about 1.33, which means that a forced to internal variance ratio of about 0.44 or greater would be judged to be significant. Results from Fig. 4 indicate that the null hypothesis would not be rejected for the 20C3M period, except for a patch with high F-ratios in the upper

troposphere over the eastern Pacific, and might be rejected over some of the eastern Pacific during the A1B period. The mass flux response to external forcing is weak during either of the 50-year periods that is being considered.

The inter-model variation $\sigma_M^2$ (Fig. 5) is comparable to internal variability in most longitudes, and exceeds internal variability over the Atlantic and western tropical Africa. It indicates the magnitude difference of mass fluxes simulated in individual models as described above. The patterns of inter-model variability are similar in the twentieth and twenty-first century periods, with somewhat changes over the Pacific.

### 3.3 Circulation changes under external forcing

We further examine the projected changes in the spatial structure and temporal evolution of the zonal circulations that result from external forcing in the twenty-first century. Figure 6 displays differences in 50-year multi-model mean mass fluxes, diabatic heating, and SST between 2050–2099 and 1950–1999, illustrating the between-period effect of external forcing. The most pronounced differences appear over equatorial Africa, the Indian Ocean and the Pacific Ocean. A pair of opposing mass flux centers is apparent (Fig. 6, top panel) over equatorial Africa and the Indian Ocean between 0 and 90°E, with $\psi$ anomalies extending throughout the troposphere. This suggests a weakening of the IOC due to external forcing, and may also indicate a westward shift of the zonal circulation over the Indian Ocean. Another pair of negative and positive $\psi$ centers is seen over the Pacific, indicating anomalous rising motion over the central Pacific and sinking motions over the western and eastern Pacific. This suggests an eastward shift of the climatological POC, resulting in a weakening of the POC uprising branch over the western Pacific and strengthening of the POC descending branch over the eastern Pacific. The blue-colored shading indicates that the changes at the centers of action are nominally statistically significant at the 5 % level.[1] In contrast, changes of mass fluxes are relatively weak over the Atlantic Ocean. The strong between-period mass flux response to external forcing differs markedly from the weak within-period response discussed above (Fig. 4). In addition, it is interesting to note that the pattern correlation between the projected circulation changes (Fig. 6, top panel) and the climatological circulation (Fig. 1, lower panel) is weakly negative (−0.18). The projected change weakens the large

---

[1] Statistical significance is assessed as a guide to interpretation. The determination of statistical significance requires the strong assumption that the collection of CMIP-3 models used in this study forms a representative sample of physically plausible comprehensive models of the physical climate system (i.e., not including representations of biogeochemical processes).
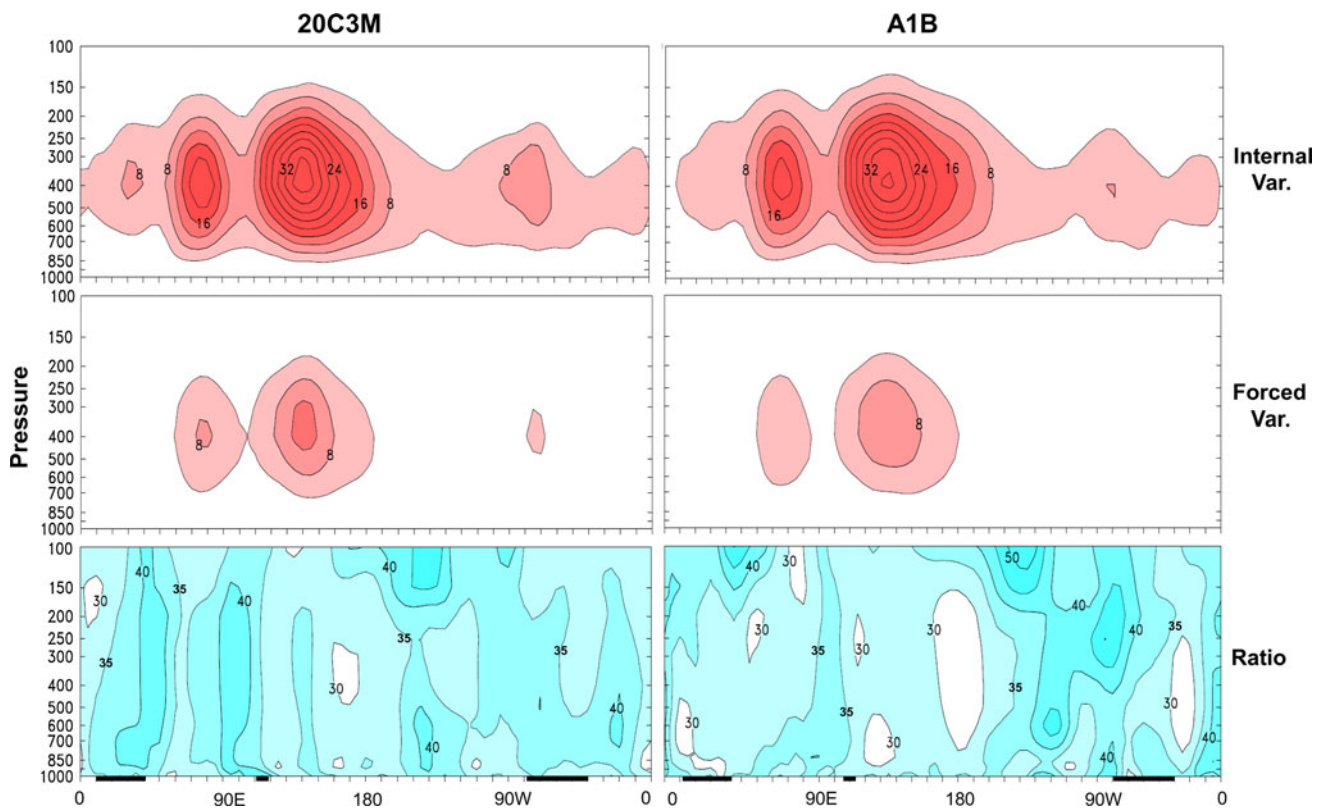
**Fig. 4** Longitude-height planes of the internal variance (*top panels*), the forced variance (*middle panels*), and the ratio of forced variance and internal variance (*bottom panels*) of annual mean mass fluxes along the equator. Results are based on the 20C3M simulations for 1950–1999 (*left panels*) and the A1B simulations for 2050–2099 (*right panels*). Contour intervals are 4.0 × 10$^{18}$ kg$^2$s$^{-2}$ for variances, and 5 % for the ratio. *Block lines* indicate land areas

**Fig. 5** Longitude-height planes of the model structure variance of annual mean mass fluxes along the equator. Results are based on the 20C3M simulations for 1950–1999 (*upper panel*) and the A1B simulations for 2050–2099 (*lower panel*). Contour interval is 4.0 × 10$^{18}$ kg$^2$ s$^{-2}$. *Block lines* indicate land areas
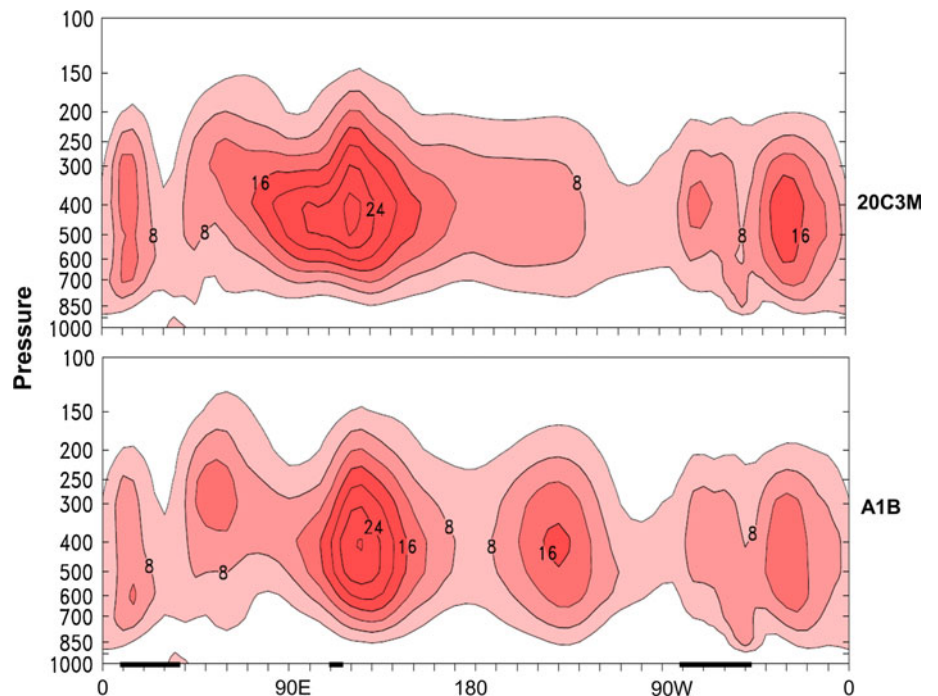
negative centre located at about 80°E, so it weakens the main zonal circulation over the Indian. It also weakens the uprising motion over the western Pacific. While the correlation coefficient is low, probably due to different circulation changes over the three oceans, it nevertheless suggests an overall weakening of the zonal circulation with global warming, generally in agreement with the theoretical point of view proposed by Held and Soden (2006).

Equatorial diabatic heating changes are consistent with the circulation changes (Fig. 6, middle panel); especially the pronounced heating anomalies located over the equatorial central Pacific and the Indian Ocean. The intensified convective heating over the equatorial central Pacific, as well as the eastward shift of the climatological POC, results in an overall strengthening of the Pacific Walker circulation. This is consistent with Vecchi and Soden (2007), who show in their Fig. 7 a tendency for strengthening of the ascending motion over the equatorial central Pacific in their multi-model mean. The changes in the POC occur in association with enhanced SST warming in the equatorial central-eastern Pacific, with large SST anomalies (about 2.1°K) apparent from 170°E to 130°W (Fig. 6, bottom panel).

Zonal circulation changes under external forcing and associated diabatic heating and SST changes simulated by individual models are generally consistent with those that are seen in the multi-model mean, with circulation changes in individual models differing mainly in magnitude (not

shown). The pattern correlations between mass flux changes in individual models and the multi-model mean exceed 0.60 for seven of nine models (Table 1), while those for diabatic heating are slightly lower but nevertheless exceed 0.60 for two-thirds of the models.

To further characterize the temporal and spatial evolution of the zonal circulations, we examine regional spatial maximum amplitudes of the mass flux field (minimum over the Indian Ocean, and maxima over the Pacific and Atlantic oceans) and their corresponding longitudes along the equator. Figure 7 presents the results over the three oceans for the multi-model mean from 1900 to 2099. The results are obtained by averaging the regional maximum amplitudes of mass fluxes and their longitudes calculated from nine individual models. Superimposed on the time series are the associated cubic trends for 1900–2099 and the linear trends for the last 100 years with enhanced external forcing. Substantial interannual variability of the circulations is clearly evident in these time series, which may be relevant to SST variations in the tropics. Weakening trends of the IOC and strengthening trends of the POC are seen throughout the 200-year period, particularly for the last 100 years with global warming, consistent with the result shown in Fig. 6. Spatial mass flux minima weaken (trend = $0.13 \times 10^9$ kgs$^{-1}$/decade with significance level $\alpha = 0.0$ %) and drift westward (trend = $-0.46°$/decade with $\alpha = 0.1$ %) over the Indian Ocean during the twenty-first century. A strengthening ($0.06 \times 10^9$ kgs$^{-1}$/decade

**Fig. 6** *Top* and *middle panels*: Longitude-height planes of the 50-year multi-model mean differences between 2050–2099 and 1950–1999 for mass fluxes ($0.5 \times 10^9$ kgs$^{-1}$, *top*) and diabatic heating ($0.1 \times 10^{-1}$ K/day, *middle*) along the equator. Negative values are cross-hatched. The anomalies significantly different from zero at the 5 % level are *blue-shaded*. *Block lines* indicate land areas. *Bottom panel*: Longitude-latitude plot of the 50-year multi-model mean SST difference (0.1 K). *Positive values* are *red-shaded*
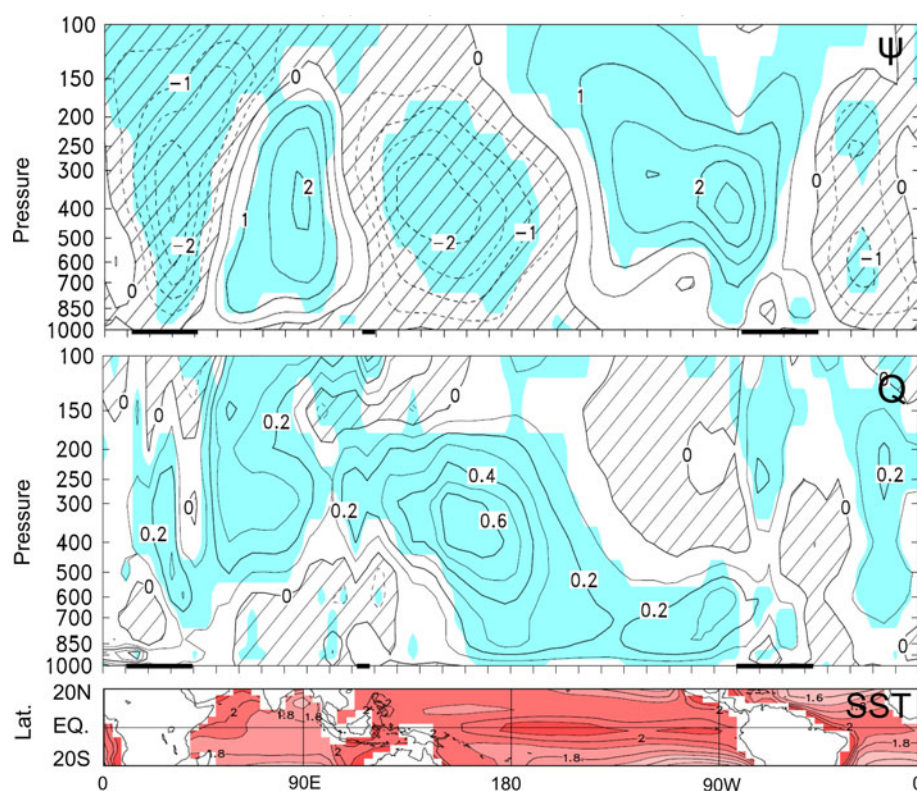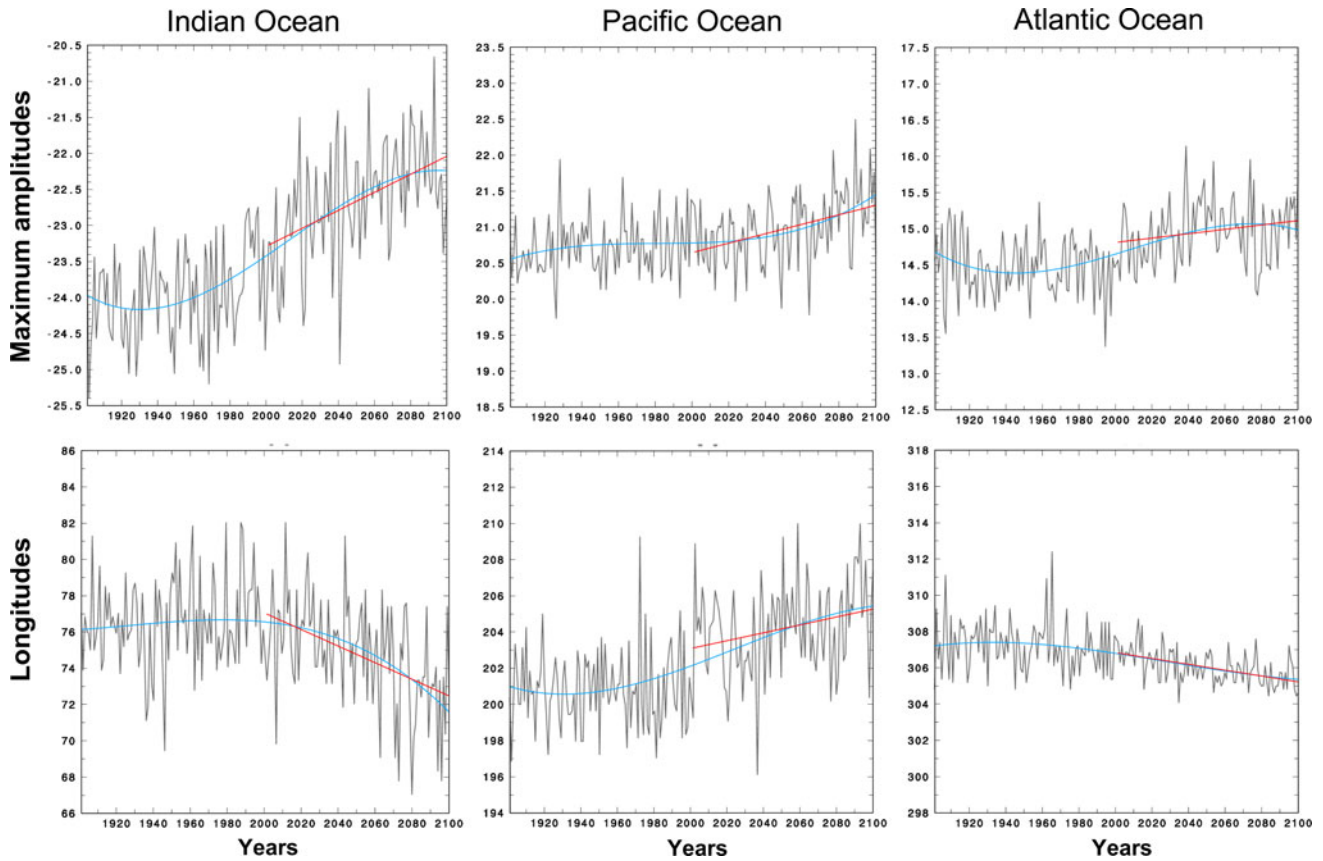
**Fig. 7** Maximum amplitudes of mass fluxes ($10^9$ kgs$^{-1}$, *upper panels*) and their longitudes (degree, *lower panels*) over the three oceans for the multi-model mean. *Blue curves* are cubic trends for 1900–2099. *Red lines* are linear trends for 2000–2099

**Table 1** Spatial pattern correlation coefficients of the 50-year changes (2050–2099 minus 1950–1999) between individual models and the multi-model mean for atmospheric mass fluxes $\psi$ and diabatic heating $Q$

| Model | $\psi$ | $Q$ |
|---|---|---|
| 1 | 0.71 | 0.69 |
| 2 | 0.67 | 0.48 |
| 3 | 0.43 | 0.41 |
| 4 | 0.46 | 0.61 |
| 5 | 0.81 | 0.68 |
| 6 | 0.79 | 0.74 |
| 7 | 0.70 | 0.61 |
| 8 | 0.66 | 0.71 |
| 9 | 0.63 | 0.41 |

with $\alpha = 0.1$ % ) and eastward shift (trend $= 0.22°$/decade with $\alpha = 0.0$ %) of maximum values of $\psi$ is seen over the Pacific Ocean. By contrast, the evolution of the AOC is relatively weak. The maximum values of $\psi$ over the Atlantic Ocean strengthen ($0.03 \times 10^9$ kgs$^{-1}$/decade with $\alpha = 4.8$ %) and drift westward (trend $= -0.16°$/decade with $\alpha = 1.2$ %) moderately.

The long-term evolution of the zonal circulations, as indicated by the regional spatial maximum amplitudes of

mass flux fields and their longitudes, varies from model to model (not shown), due probably to large inter-model mass flux variations as described above. Table 2 lists the linear trends of spatial maximum amplitudes for $\psi$ and their longitudes from 2000 to 2099 over the three oceans for the multi-model mean and nine individual models. The mass flux trends are subject to considerable uncertainty, with wide differences in trends apparent across the models. Nevertheless, the evolution features seen from the multi-

**Table 2** Linear trends of spatial maximum amplitudes of mass fluxes ($10^9$ kgs$^{-1}$/decade) and trends of the corresponding longitudes (degree/decade) for 2000–2099 over the three oceans

| Model | Indian Ocean | | Pacific Ocean | | Atlantic Ocean | |
|---|---|---|---|---|---|---|
| | Min. | Long. | Max. | Long. | Max. | Long. |
| Mean | **0.13** | **−0.46** | **0.06** | **0.22** | **0.03** | **−0.16** |
| 1 | −0.05 | **−2.06** | **0.08** | −0.12 | **0.29** | **−0.17** |
| 2 | −0.05 | 0.29 | 0.02 | −0.43 | **−0.11** | 0.01 |
| 3 | **−0.24** | 0.36 | **0.13** | **−1.31** | **−0.22** | **−0.17** |
| 4 | **0.08** | **−1.07** | **0.30** | 0.13 | 0.02 | **−0.18** |
| 5 | **0.64** | **−1.55** | **−0.27** | **0.48** | **0.14** | **−0.37** |
| 6 | **0.49** | **−0.25** | **−0.17** | **1.13** | **0.17** | **−0.29** |
| 7 | **0.11** | **−0.56** | **−0.05** | **0.97** | **0.06** | **−0.29** |
| 8 | **0.11** | 0.80 | **0.51** | **0.44** | **−0.14** | 0.02 |
| 9 | 0.03 | −0.06 | 0.03 | **0.70** | **0.08** | −0.01 |

The results include trends for the multi-model mean and nine individual models. Bold values indicate those that are statistically significant at the 5 % level

model mean (Fig. 7) appear in about two-thirds of the models. In addition, about half of the trends are statistically significant at the 5 % level.

## 4 Seasonal cycle of the zonal circulation

### 4.1 Structure of zonal circulations and diabatic heating

The thermally driven circulation has a seasonal cycle as a consequence of the seasonal variation in the energy exchange between the atmosphere and ocean. Here we examine the seasonal cycle of the equatorial zonal circulation. The sequence of events is indicated by northern seasons, with March–May (MAM) defined as spring, June–August (JJA) as summer, September–November (SON) as fall, and December–February (DJF) as winter. The equatorial zonal circulations for the four seasons (not shown) generally resemble those obtained using all calendar months (Fig. 1), with three major components over the three oceans. The atmospheric mass fluxes extend deeply throughout the troposphere for all seasons, with the centers of action located in the mid-troposphere. However, circulation differences also appear in the four seasons, including variations in intensity and accompanying longitudinal shifts.

Figure 8 displays longitude-time sections of climatological monthly means of vertically averaged mass fluxes between 300 and 600 hPa, the more prominently visible areas. The IOC, indicated by the negative mass flux center over the equatorial Indian Ocean, features a striking contrast between JJA and DJF that is probably related to the seasonal variation of the Indian monsoon (e.g., Peixoto and Oort 1992, Chapter 7). In contrast, the magnitudes of the POC and the AOC, indicated by the positive centers over the corresponding oceans, are relatively stronger in summer and winter than those in spring and fall. The mass flux centers migrate zonally during the course of the year,

especially for the centers of action corresponding to the POC and AOC, shifting westward from northern winter to summer and then returning eastward from northern summer to winter. Over the Pacific, the positive center of action for mass flux migrates 30–40° longitudinally during the year. It locates around 160–170°W over the central Pacific in JJA, shifts eastward and reaches 130°W over the eastern Pacific in DJF. The center shifts westward subsequently during the next half of the year. The AOC mass flux center also migrates zonally, between 50 and 30°W, but migration is less apparent for the IOC. Similar features are seen in the reanalysis and in the multi-model mean. The differences between the two types of products occur mainly in the mass flux intensity, with generally lower values in the multi-model mean compared to the reanalysis.

The seasonal zonal migration of the POC and AOC is accompanied by a corresponding seasonal migration of atmospheric diabatic heating (Fig. 9). Local heating variations dominate over the Indian Ocean (upper panel), accompanying the local variation of the IOC as described above. Strong heating values are also seen over equatorial South America during the northern winter season, consistent with Hoskins et al. (1989). The seasonal cycle is reasonably well reproduced in the multi-model mean (lower panel), though the modeled result is generally smoother than that in the reanalysis perhaps reflecting the fact that multi-model averaging removes much of the sampling variability that causes uncertainty in observationally derived products that may be responsible for some of the small-scale detail seen in the upper panel of Fig. 9.

The seasonal features of mass flux and diabatic heating as obtained from the multi-model mean remain dominant in most models individually (not shown). The relative agreements of the seasonal mean circulations in individual models with the corresponding averages of the two reanalysis based values are presented in Fig. 10. Spatial
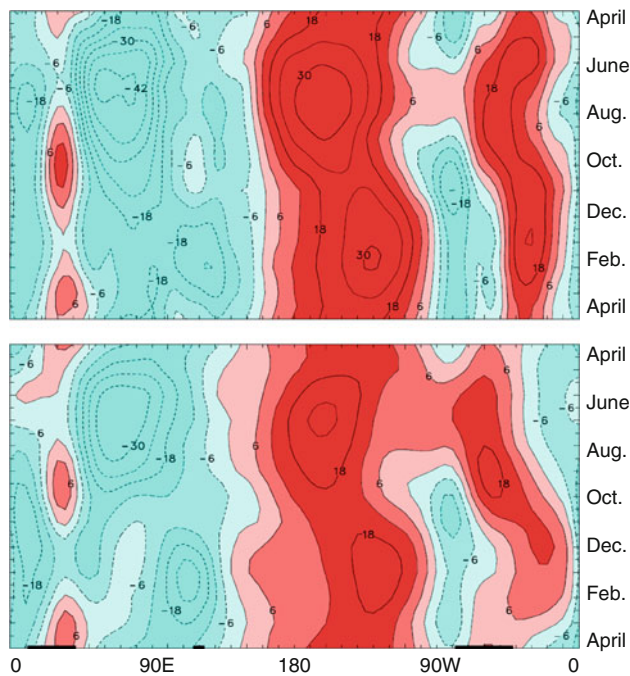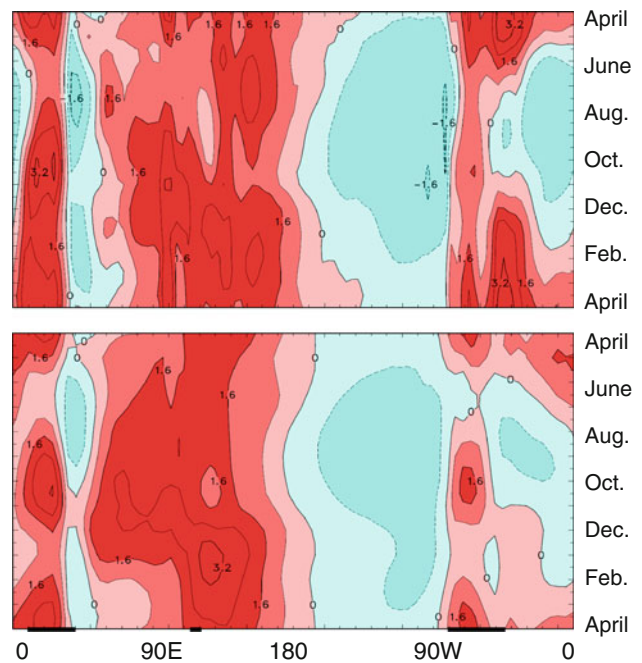
**Fig. 8** Longitude-time sections of climatological monthly means of vertically averaged mass fluxes between 300 and 600 hPa along the equator for the mean of NCEP and ERA-40 reanalyses from 1957 to 2001 (*upper panel*) and the multi-model mean from 1950 to 1999 (*lower panel*). Contour interval is $6.0 \times 10^9$ kg s$^{-1}$. *Block lines* indicate land areas



**Fig. 9** As in Fig. 8, but for the diabatic heating. Contour interval is $0.8 \times 10^{-1}$ K/day

pattern correlations of mass fluxes exceed 0.70 for most models, especially in northern summer and winter. However, compared to reanalysis results, variance ratios are generally lower than one, suggesting smooth mass flux patterns with less spatial variance than observed. In addition, in all seasons, the mean model is again seen to perform better than individual models.

### 4.2 Internal and forced variances

The seasonal features of the internal, forced and model structure related variances of the mass flux are generally similar to those based on the annual mean (Figs. 4, 5), with the most pronounced variability apparent mainly over the Indian Ocean and the western-central Pacific but with magnitude that varies with season. Figure 11 displays longitude-time sections of 300–600 hPa vertically averaged variances for the 20C3M simulations from 1950 to 1999. As for the annual mean, the total variance is dominated by internal variability and differences in model structure. The internal and forced variability is higher in northern cold seasons (October through March) than in warm seasons (April–September). In contrast, $\sigma_M^2$ remains high throughout the year over the western Pacific, and is relatively larger in northern warm seasons than in cold

seasons over the Indian Ocean. Similar results are obtained from the A1B simulations (not shown).

### 4.3 Changes of circulations under external forcing

Figure 12 displays the monthly changes in the 50-year multi-model means of 300–600 hPa vertically averaged mass flux and diabatic heating between 2050–2099 and 1950–1999, corresponding to the vertically distributed annual mean result presented in Fig. 6. The external forcing results in mass flux changes throughout the year, including a weakening and westward shift of the climatological IOC and an eastward shift of the POC. However, the opposing mass flux changes over the Pacific are more prominent in the northern warm season, while the increase of mass flux over the Indian Ocean dominates in the northern cold season. The forced change in the AOC is weak throughout the year, except that around December. The seasonal diabatic heating changes (Fig. 12, lower panel) are responsible for the corresponding mass flux changes, especially for the circulation changes over the Pacific. The seasonal mass flux and diabatic heating changes are generally consistent across individual models (not shown).

## 5 ENSO influence on the zonal circulation

As noted in the introduction, recent studies demonstrate that the frequency of central Pacific El Niño events

**Fig. 10** As in Fig. 3, but for the mass fluxes for the four seasons
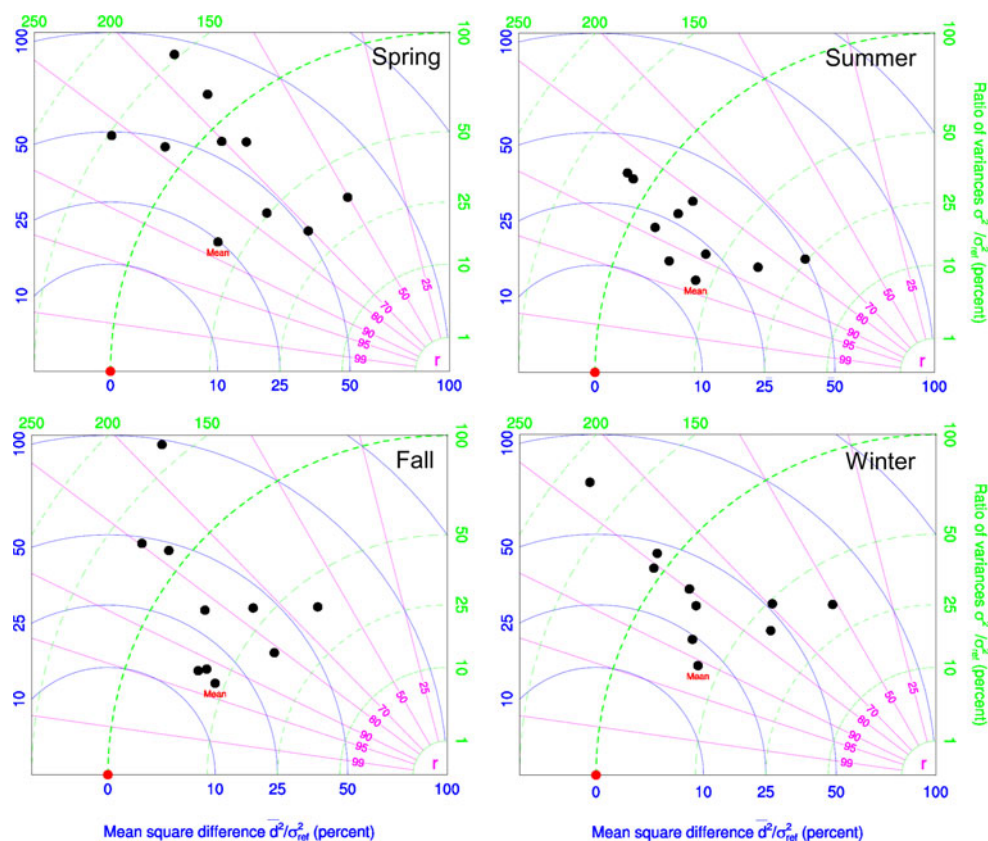
increased during the late twentieth century, a phenomenon that is also seen in several global warming simulations (e.g., Trenberth and Stepaniak 2001; and Yeh et al. 2009). The CP-El Niño is characterized by increased SST anomalies in the central equatorial Pacific, accompanied by anomalous cooling in the east and west (Ashok and Yamagata 2009), resulting in circulation changes over the tropical Pacific. On the other hand, ENSO projections remain uncertain, as has also been highlighted in recent studies (e.g., Leloup et al. 2008; Collins et al. 2010; and Vecchi and Wittenberg 2010). Here, we examine the influence of ENSO on annual mean mass flux in the model simulations.

The ENSO variability considered here is represented by the first EOF of the model-simulated tropical Pacific annual mean SST anomalies that remain after removing the cubic trend at each grid point. The EOF analysis is performed for the tropical Pacific region bounded by 20°S–20°N and 120°E–70°W, and is calculated for each 100-year model simulation. The first EOF patterns obtained from individual models resemble those reported in previous studies (e.g., Merryfield 2006). The leading EOF accounts for 47.8 and 45.6 % of the total annual mean SST variance, averaged across 27 model simulations, for the 100-year 20C3M and 100-year A1B simulations respectively. The leading mode

is well separated from subsequent EOFs as per the criterion of North et al. (1982).

We use values of the standardized principal component time series of the ENSO mode greater than one in absolute value to define ENSO events. Accordingly, we obtain 198 El Niño, 208 La Niña and 944 neutral years for the 27 model simulations for 1950–1999. Likewise, we identify 191 El Niño, 202 La Niña and 957 neutral years for 2050–2099. We then calculate averaged mass fluxes for El Niño, La Niña and neutral years for each model, and examine spatial maximum amplitudes of the composite mass fluxes over the three oceans and their corresponding longitudes.
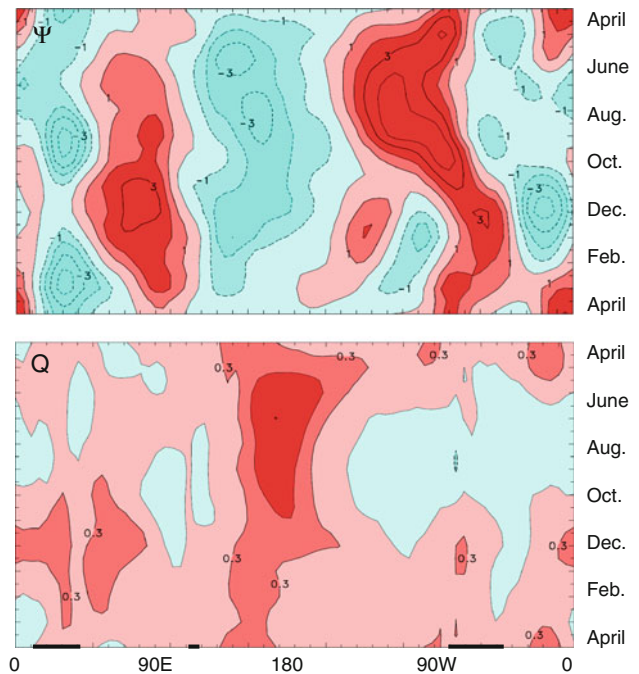
Table 3 lists the multi-model mean results for different composites during the two periods, with the secular trend due to the anthropogenic forcing remaining in the stream-function. This allows us to analyze both the ENSO effects on mass fluxes and the effects of external forcing on the zonal circulation for the three different composites. For each period, the mass flux circulation over the equatorial Pacific weakens and shifts eastwards during El Niño compared to neutral years, as expected. The circulation weakens and shifts westward over the Indian Ocean, while it strengthens and shifts westward slightly over the Atlantic Ocean. The circulations change in the opposite sense over
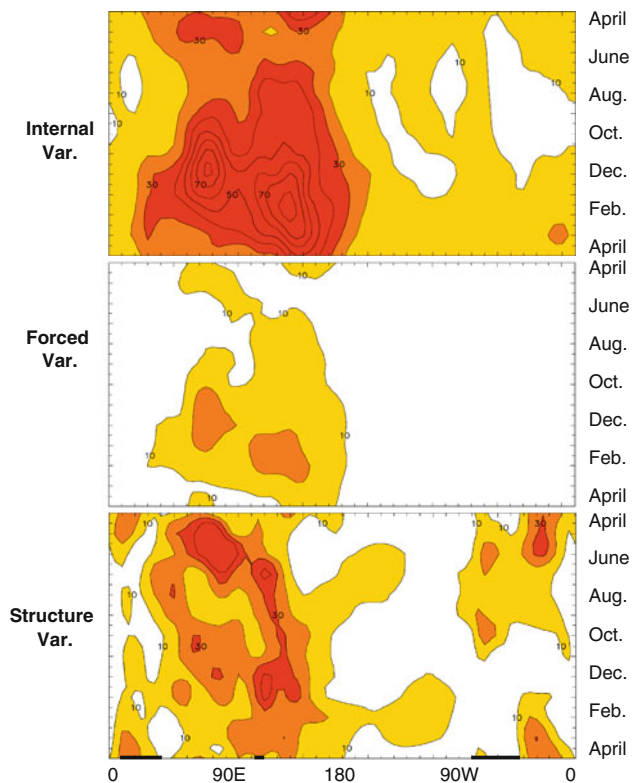
**Fig. 11** Longitude-time sections of 300–600 hPa vertically averaged internal variances (*top panel*), forced variances (*middle panel*), and model structure variances (*bottom panel*) for the multi-model mean from 1950 to 1999. Contour interval is $10.0 \times 10^{18}$ kg$^2$s$^{-2}$. *Block lines* indicate land areas



**Fig. 12** As in Fig. 8, but for the 50-year multi-model mean differences between 2050–2099 and 1950–1999 for mass fluxes ($1.0 \times 10^9$ kgs$^{-1}$, *upper panel*) and diabatic heating ($0.3 \times 10^{-1}$ K/day, *lower panel*)

the three oceans during La Niña events. These features are clearly evident in both periods, except a westward shift of the mass flux center is apparent over the Indian Ocean in the La Niña composite for 2050–2099.

We then compare 2050–2099 and 1950–1999 results to evaluate the effects of external forcing on the zonal circulation for the different composites. The El Niño, La Niña and neutral composites all show similar changes, although the intensity of changes differs somewhat (Table 3). Consistent with the results shown in Figs. 6 and 7, mass fluxes strengthen over the Pacific and Atlantic oceans with global warming, and weaken over the Indian Ocean. The mass flux centers migrate eastward over the Pacific and westward over the Indian and Atlantic oceans. In addition, the forced changes in mass flux maximum amplitudes and their longitudes over the equatorial Pacific are larger in neutral years than those in ENSO years (Table 3). These results suggest that the changes in the equatorial zonal circulations under external forcing (Fig. 6) are associated not only with ENSO related SST and atmospheric diabatic heating anomalies but also with broad SST and heating changes in the tropics. Overall, the changes in ENSO related mass fluxes under external forcing are modest.

Figure 13 displays longitude-height planes of multi-model mean mass flux anomalies, with respect to the corresponding 50-year climatology, for the El Niño composites over 1950–1999 and 2050–2099, and the difference between them. The El Niño related circulation anomalies are dominated by an anomalously negative mass flux cell over the equatorial Pacific and two positive $\psi$ cells overlying the Indian Ocean and from the Amazon region to the eastern equatorial Atlantic, respectively. Thus the climatological POC and IOC are generally weakened during the El Niño events, while the climatological AOC is strengthened. Similar anomalies of opposite sign are seen in the La Niña composite (not shown). These are also the canonical features in association with the ENSO variability (e.g., Peixoto and Oort 1992).

The ENSO related mass flux anomalies are of the same order of magnitude as in the 50-year mean mass flux responses to external forcing between 2050–2099 and 1950–1999 (Fig. 6, top panel), and bear some resemblance to the mass flux responses over the western Pacific and the Indian Ocean. This similarity may indicate that the mean forced response is affected by an El Niño-like warming pattern as seen in several models (e.g., Merryfield 2006) and pointed out in previous studies (e.g., Knutson and Manabe 1995; Meehl and Washington 1996; Meehl et al. 2007b). Yet, notable differences between the forcing response and the ENSO related mass flux anomalies are

**Table 3** Spatial maximum amplitudes of composite mass fluxes ($10^9$ kgs$^{-1}$) and their longitudes (degree) for 1950–1999 and 2050–2099 over the three oceans

| Comps. | Indian Ocean | | Pacific Ocean | | Atlantic Ocean | |
|---|---|---|---|---|---|---|
| | Min. | Long. | Max. | Long. | Max. | Long. |
| *1950–1999* | | | | | | |
| La Niña | −25.0 | 77.2 | 20.7 | 200.6 | 12.9 | 307.2 |
| Neutral | −23.2 | 75.6 | 19.9 | 201.1 | 14.2 | 306.1 |
| El Niño | −21.6 | 74.4 | 18.8 | 207.2 | 15.7 | 305.6 |
| *2050–2099* | | | | | | |
| La Niña | −24.3 | 71.7 | 20.8 | 203.9 | 13.4 | 305.6 |
| Neutral | −21.1 | 75.0 | 20.7 | 207.2 | 14.8 | 305.0 |
| El Niño | −19.2 | 72.2 | 19.1 | 211.7 | 16.7 | 303.9 |

**Fig. 13** Longitude-height planes of multi-model mean mass flux anomalies with respect to the corresponding 50-year climatology for the El Niño composites over 1950–1999 (*top*) and 2050–2099 (*middle*), and the difference between 2050–2099 and 1950–1999 (*bottom*). The contour interval is 0.5 × $10^9$ kgs$^{-1}$
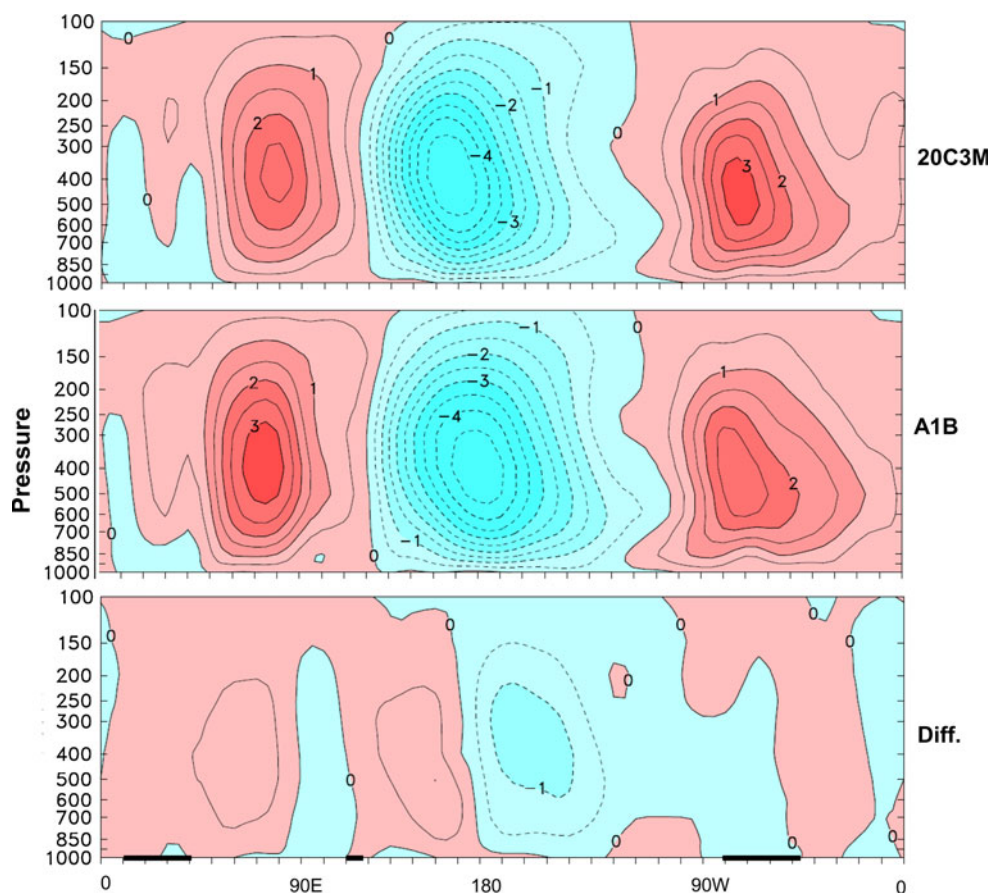


also apparent over the equatorial eastern Pacific. Several recent studies demonstrated that physical mechanisms driving tropical Pacific climate change depart from that of the ENSO variability, in particular the equatorial thermocline has a strong negative feedback on global warming timescales that prevents the equatorial Pacific from becoming El Niño-like (e.g., DiNezio et al. 2009, 2010).

The ENSO related mass flux anomalies with respect to the corresponding 50-year mean background are similar in the two periods, with slight differences mainly over the central-western Pacific and the western Indian Ocean (Fig. 13, lower panel). Thus the changes in ENSO related mass fluxes under the anthropogenic forcing are modest between the two 50-year periods, compared to either the substantial mass flux difference between the two climatological means (Fig. 6) or the ENSO related mass flux anomalies (Fig. 13). Recently, Yeh et al. (2009) reported that the CP-El Niño became more common than the canonical EP-El Niño during the late twentieth century, with two opposing circulation anomalies over the

equatorial eastern and western Pacific (Ashok and Yamagata 2009). However, the EP-El Niño and CP-El Niño related anomalies were constructed as deviations from the same 1854–2006 climatology in Yeh et al. (2009). It remains to explore the extent to which the observed circulation anomalies may be related to interannual variability or to the secularly forced trend.

# 6 Summary

The tropical zonal circulation impacts the global climate and is closely related to the tropical monsoon and ENSO. In this study, we analyze the structure and variability of the equatorial zonal circulation using the NCEP and ERA-40 reanalyses and the CMIP3 climate model archive. We evaluate the modeled circulations by comparing them with those derived from the reanalyses. We then examine the variability of the circulation, its changes with global warming, and the associated thermodynamic maintenance.

The equatorial zonal circulation is characterized by the thermally driven divergent component of atmospheric flow and involves three major components over the Pacific, the Indian, and the Atlantic oceans, indicated by mass flux centers of action over the three oceans. The mass flux centers migrate zonally throughout the year, particularly those corresponding to the POC and AOC, shifting westward from northern winter to summer and returning eastwards from northern summer to winter. The magnitudes of the POC and AOC mass fluxes are higher in JJA and DJF than those in MAM and SON. Seasonal migration of the Indian Ocean circulation is less evident, but the magnitude of IOC mass flux does vary seasonally, strengthening in JJA and weakening in DJF. The three circulations are directly supported by the corresponding diabatic heating extending deeply throughout the troposphere, with heating centers apparent in the mid-troposphere. Most models capture the annual and seasonal features of the circulations that are seen in reanalyses, and the associated heating structures, reasonably well, as does the multi-model mean. As has also been found in other research, the multi-model mean reproduces the observed climatology better than any individual model, as indicated by the spatial pattern correlation and mean square difference of the mass flux and the diabatic heating compared to the reanalysis based values.

The model-simulated transient mass flux response to external forcing during either of the two 50-year periods 1950–1999 based on the 20C3M simulations and 2050–2099 based on the A1B simulations, is weak. However, the mass flux responses differ substantially between the two periods. The responses of the circulations to external forcing are dominated by mass flux anomalies over the Pacific and Indian oceans. Enhanced SST warming is apparent in the equatorial central-eastern Pacific, together with pronounced heating anomalies located over the equatorial central Pacific, which drives anomalous rising motion over the central Pacific and sinking motions in the west and east. This weakens the rising branch of the Pacific Walker circulation over the western Pacific and strengthens the descending branch over the eastern Pacific, leading to an overall strengthening of the Walker circulation. It also suggests an eastward shift of the climatological POC. The zonal circulation weakens and shifts westwards over the Indian Ocean with global warming, whereas the circulation strengthens and shifts westwards slightly over the Atlantic Ocean. Confidence in the projected circulation changes is high for the multi-model mean. The pattern of circulation changes is weakly anti-correlated with the climatological circulation, suggesting a general weakening of the zonal circulation with global warming, in agreement with the theoretical point of view proposed by Held and Soden (2006). The changes of the POC are also consistent with Vecchi and Soden (2007). In addition, the mass flux changes over the Pacific are more prominent in the northern warm season (April-September), while the increase of mass flux over the Indian Ocean dominates in the northern cold season (October–March). The forced change over the Atlantic Ocean is generally weak throughout the year.

Linear trends of the forced circulation changes, as characterized by regional spatial maximum amplitudes of mass fluxes and their longitudes over the three oceans, are statistically significant at the 5 % level for 2000–2099 for the multi-model mean. However, wide differences of the trends are apparent across the models because there is strong model dependence in the climatological representation of the circulations and because internal variability of mass flux is high for each model.

The ENSO related mass flux anomalies are of the same order of magnitude as the responses in 50-year mean mass flux to external forcing between 2050–2099 and 1950–1999. The anomalies bear some resemblance to the forcing responses over the equatorial western Pacific and the Indian Ocean, and with differences between them over the equatorial eastern Pacific. The ENSO related mass flux changes projected by models are modest. Over the equatorial Pacific, the changes of mass flux maximum amplitudes and their corresponding longitudes are larger in neutral years than those in ENSO years. The forced changes in the equatorial zonal circulation are associated with broad SST and atmospheric diabatic heating changes in the tropics.

# References

Ashok K, Yamagata T (2009) Climate change: the El Niño with a difference. Nature 416:481–484

Betts AK (1998) Climate-convection feedbacks: some further issues. Climatic Change 39:35–38

Betts AK, Ridgway W (1989) Climatic equilibrium of the atmospheric convective boundary layer over a tropical ocean. J Atmos Sci 46:2621–2641

Boer GJ, Lambert S (2001) Second-order space-time climate difference statistics. Climate Dyn 17:213–218

Clarke AJ, Lebedev A (1997) Interannual and decadal changes in equatorial wind stress in the Atlantic, Indian, and Pacific Oceans and the eastern ocean coastal response. J Climate 10:1722–1729

Cobb KM, Charles CD, Hunter DE (2001) A central tropical Pacific coral demonstrates Pacific, Indian, and Atlantic decadal climate connections. Geophys Res Lett 28:2209–2212

Collins M et al (2010) The impact of global warming on the tropical Pacific ocean and El Niño. Nat Geosci 3:391–397

Deser C, Phillips AS, Hurrell JW (2004) Pacific interdecadal climate variability: linkages between the tropics and the North Pacific during boreal winter since 1900. J Climate 17:3109–3124

DiNezio PN, Clement AC, Vecchi GA, Soden BJ, Kirtman BP, Lee SK (2009) Climate response of the equatorial pacific to global warming. J Climate 22:4873–4892

DiNezio P, Clement A, Vecchi G (2010) Reconciling differing views of tropical Pacific climate change. Eos Trans 91(16):141. doi:10.1029/2010EO160001

Gastineau G, Li L, Treut HL (2009) The Hadley and Walker circulation changes in global warming conditions described by idealized atmospheric simulations. J Climate 22:3993–4013

Graham NE (1994) Decadal-scale climate variability in the tropical and North Pacific during the 1970s and 1980s: observations and model results. Climate Dyn 10(3):135–162

Held IM, Soden BJ (2006) Robust responses of the hydrological cycle to global warming. J Clim 19:5686–5699

Hildebrand FB (1956) Introduction to numerical analysis. McGraw-Hill Book Company, INC., New York, 511 pp

Hoskins BJ, Hsu HH, James IN, Masutani M, Sardeshmukh PD, White GH (1989) Diagnostics of the global atmospheric circulation based on ECMWF analyses 1979–1989. WCRP-27, 217 pp

Kistler R et al (2001) The NCEP-NCAR 50-year reanalysis: monthly means CD-ROM and documentation. Bull Am Meteor Soc 82:247–268

Knutson TR, Manabe S (1995) Time-mean response over the tropical Pacific due to increased $CO_2$ in a coupled ocean–atmosphere model. J Clim 8:2181–2199

Leloup J, Lengaigne M, Boulanger JP (2008) Twentieth century ENSO characteristics in the IPCC database. Clim Dyn 30:227–291

Lu J, Vecchi GA, Reichler T (2007) Expansion of the Hadley cell under global warming. Geophys Res Lett 34:L06805. doi:10.1029/2006GL028443

Ma J, Li J (2008) The principal modes of variability of the boreal winter Hadley cell. Geophys Res Lett 35:L01808. doi:10.1029/2007GL031883

Meehl GA, Washington WM (1996) El Niño-like climate change in a model with increased atmospheric CO2 concentrations. Nature 382:56–60

Meehl GA, Covey C, Delworth T, Latif M, McAvaney B, Mitchell JFB, Stouffer RJ, Taylor KE (2007a) The WCRP CMIP3 multimodel dataset: a new era in climate change research. Bull Am Meteor Soc 88:1383–1394

Meehl GA et al (2007b) Global climate projections, in climate change 2007: the physical science basis—contribution of working group I to the fourth assessment report of the intergovernmental panel on climate change. Cambridge University Press, New York, pp 747–845

Merryfield WJ (2006) Changes to ENSO under CO2 doubling in a multi-model ensemble. J Clim 19:4009–4027

Mitas CM, Clement A (2005) Has the Hadley cell been strengthening in recent decades? Geophys Res Lett 32:L03809. doi:10.1029/2004GL021765

Mitas CM, Clement A (2006) Recent behavior of the Hadley cell and tropical thermodynamics in climate models and reanalyses. Geophys Res Lett 33:L01810. doi:10.1029/2005GL024406

Nigam S (1994) On the dynamical basis for the Asian summer monsoon rainfall—El Niño relationship. J Climate 7:1750–1771

North GR, Bell TL, Cahalan RF, Moeng FJ (1982) Sampling errors in the estimation of empirical orthogonal functions. Mon Wea Rev 110:699–706

Peixoto J, Oort A (1992) The physics of climate. AIP, New York, 520 pp

Quan XW, Diaz HF, Hoerling MP (2004) Change of the Hadley circulation since 1950. In: Diaz HF, Bradley RS (eds) The hadley circulation: past, present, and future. Springer, New York, pp 85–120

Sugi M, Noda A, Sato N (2002) Influence of the global warming on tropical cyclone climatology: an experiment with the JMA global model. J Meteor Soc Jpn 80:249–272

Tanaka HL, Ishizaki N, Kitoh A (2004) Trend and interannual variability of Walker, monsoon and Hadley circulations defined by velocity potential in the upper troposphere. Tellus A 56:250–269

Ting MF, Kushnir Y, Seager R, Li C (2009) Forced and internal twentieth-century SST trends in the North Atlantic. J Climate 22:1469–1481

Trenberth KE, Hurrell JW (1994) Decadal atmosphere-ocean variations in the Pacific. Climate Dyn 9:303–319

Trenberth KE, Stepaniak DP (2001) Indices of El Nino evolution. J Clim 14:1697–1701

Uppala SM et al (2005) The ERA-40 re-analysis. Quart J R Meteor Soc 131:2961–3012

Urban FE, Cole JE, Overpeck JT (2000) Influence of mean climate change on climate variability from a 155-year tropical Pacific coral record. Nature 407:989–993

Vecchi GA, Soden BJ (2007) Global warming and the weakening of the tropical circulation. J Clim 20:4316–4340

Vecchi GA, Wittenberg AT (2010) El Niño and our future climate: where do we stand? Clim Change 1:260–270

Vecchi GA, Soden BJ, Wittenberg AT, Held IM, Leetmaa A, Harrison MJ (2006) Weakening of tropical Pacific atmospheric circulation due to anthropogenic forcing. Nature 441:73–76

von Storch H, Zwiers FW (1999) Statistical analysis in climate research. Cambridge University Press, Cambridge, 494 pp

Walker CC, Schneider T (2006) Eddy-influences on Hadley circulations: simulations with an idealized GCM. J Atmos Sci 63:3333–3350

Yeh SW, Kug JS, Dewitte B, Kwon MH, Kirtman BP, Jin FF (2009) El Niño in a changing climate. Nature 461:511–514

Yu B, Boer GJ (2002) The roles of radiation and dynamical processes in the ElNiño-like response to global warming. Clim Dyn 19:539–553

Yu B, Zwiers F (2010) Changes in equatorial atmospheric zonal circulations in recent decades. Geophys Res Lett 37:L05701. doi:10.1029/2009GL042071

Zhang M, Song H (2006) Evidence of deceleration of atmospheric vertical overturning circulation over the tropical Pacific. Geophys Res Lett 33:L12701. doi:10.1029/2006GL025942

Zhang Y, Wallace JM, Battisti DS (1997) ENSO-like interdecadal variability: 1900–1993. J. Climate 10:1004–1020

Zwiers FW (1996) Interannual variability and predictability in an ensemble of AMIP climate simulations conducted with CCC GCM2. Clim Dyn 12:825–847